COMPUTATIONAL PREDICTIONS OF THE PERFORMANCE OF WRIGHT "BENT END" PROPELLERS

Xiangyu Wang

Robert L. Ash

Department of Aerospace Engineering

Old Dominion University, Norfolk, VA 23529

and

Percy J. Bobbitt

Eagle Aeronautics

Abstract

Computational analysis of two 1911 Wright brothers " Bent End " wooden propeller reproductions have been performed and compared with experimental test results from the Langley Full Scale Wind Tunnel.[1] The purpose of the analysis was to check the consistency of the experimental results and to validate the reliability of the tests. This report is one part of the project on the propeller performance research of the Wright "Bent End" propellers, intend to document the Wright brothers' pioneering propeller design contributions. Two computer codes were used in the computational predictions. The FLO_MG Navier-Stokes code [2] is a CFD code based on the Navier-Stokes Equations. It is mainly used to compute the lift coefficient and the drag coefficient at specified angles of attack at different radii [3]. Those calculated data are the intermediate results of the computation and a part of the necessary input for the Propeller Design Analysis Code [4] (based on Adkins and Libeck method) , which is a propeller design code used to compute the propeller thrust coefficient, the propeller power coefficient and the propeller propulsive efficiency.

Nomenclature

x, y, z = physical direction

x_{le} , z_{le} = the coordinate of the leading edge at the physical domain

x_{te} , z_{te} = the coordinate of the trailing edge at the physical domain

z_a = an intermediate variable at the physical domain for the convenience of domain conversion

$x_{\_bar}$, $y_{\_bar}$, $z_{\_bar}$ = computational direction

ϕ = flow angle

c = blade section chord

α = angle of attack

R = propeller tip radius

r = radial coordinate

ξ = nondimensional radius = r/R

C_l = blade section lift coefficient

C_d = blade section drag coefficient

C_P = propeller power coefficient

C_T = propeller thrust coefficient

J = propeller advance ratio

RPM = rotational speed of the propeller

V = forward velocity

P = dynamic pressure

η = propeller propulsive efficiency

Introduction

The Wright brothers spent a great deal of time and resources in trying to design high efficient, practical wooden propellers. As we approach the 100th anniversary of the Wright brothers' first controlled, powered flight, it is important to recognize that perfecting efficient propellers was a key contribution to the Wright brothers' success. Two Wright brothers bent end wooden propeller reproductions were built for the testing in the Langley Full Scale wind tunnel. [1] Measurements have demonstrated the effectiveness of their ingenious use of Wilbur Wright's blade element theory, exploiting large diameter propellers, turning at low rotational speeds. Their " optimized " propeller designs utilized rearward blade sweep and incorporated a type of composite fiber tip covering to produce propellers with maximum efficiencies above 85 percent at nominal advance ratios slightly above one. Since the maximum efficiencies are as good as or even better than modern propeller designs, it is really surprising. To confirm the accuracy of the experiment results, computational predictions were done for comparison, using the FLO_MG Navier-Stokes code [2] and the Propeller Design Analysis Code [4]. The initial conditions are the same as the test conditions, and most of the critical intermediate results were checked and corrected to guarantee accuracy of the subsequent calculations and the final results.

Procedure

A. Calculations on the FLO_MG Navier-Stokes code

The FLO_MG is a code used to acquire the blade section lift coefficient and the drag coefficient. [2,3] The dimensionless coordinates in the computational domain, the specified angle of attack, Mach numbers, and Reynolds numbers are all necessary input for the code. The mesh plots are intermediate results, the accuracy of which will ensure the meaning of the later work.

(1) Dimensionless conversion of the coordinates to computational domain

The original geometric parameters of the propeller were obtained from the careful measurements at NASA Langley Research Center. They include the coordinates of the points at the edge of each cross section, the area of each cross section, and the perimeter of each section. Ten blade cross sections radii were selected for profile data. Their nondimensional radiuses are 0.20, 0.30, 0.4, 0.5, 0.6, 0.7, 0.8, 0.9, 0.96 and 1.0, while the whole propeller blade radius is 51 in (4.25 ft). Figures 1.01 to 1.08 are plots of various blade cross section from $\xi = 0.2$ to $\xi = 0.9$ (The coordinate where $\xi = 0.96$ and $\xi = 1$ is not available). Each blade section was represented as pairs of x and z coordinates in a data file, which is described by these x_i, z_i "points". The local chord length is computed by calculating all combinations of $\sqrt{(x_i - x_j)^2 + (z_i - z_j)^2}$ for all i and j, and finding the maximum length from these calculations. The relevant two points making the chord represented the position of the leading edge and trailing edge. To change the two-dimensional propeller blade cross-sections into dimensionless airfoils, with a chord length of unity and with the chord reference plane aligned with the $x_{\_bar} - y_{\_bar}$ plane ($z_{\_bar} = 0$), the equations (1)-(5) were used to effect the conversion.

$$c = \sqrt{(z_{le} - z_{te})^2 + (x_{le} - x_{te})^2} \qquad \text{------------------(1)}$$

$$\phi = \tan^{-1}\frac{z_{le} - z_{te}}{x_{le} - x_{te}} \qquad \text{-----------------(2)}$$

$$z_a = (x - x_{te}) * \tan\phi + z_{te} \qquad \text{-----------------(3)}$$

$$x_{\_bar} = \frac{(x_{le} - x)/\cos - (z - z_a) * \sin\phi}{c} \qquad \text{-----------------(4)}$$

$$z_{\_bar} = \frac{(z - z_a) * \cos\phi}{c} \qquad \text{-----------------(5)}$$

Figures 2.01 to 2.08 are the converted plots of the cross sections for ξ =0.2 to ξ =0.9 based on Equations (1)-(5). In the new plots, the dimensionless top and bottom surface are located at the positions according to functions of the new dimensionless horizontal x-coordinate ($x_{\_bar}$). Since in the new coordinate system, each section was of unit length and no longer used the airflow direction as the reference horizontal direction, the flow approached the section with an angle of attack corresponding to the actual orientation of the propeller section to the original coordinate system. The angles at which the air will strike each airfoil section had to be specified.

(2) Reynolds number and Mach number

Eagle Aeronautics provided the Mach number vs. Reynolds number in plot, shown in Figure 3.01 and Figure 3.02. From Figure 3.01, the Mach number at each cross section can be gotten directly. From the Figure 3.02, the Reynolds number over the chord length can be calculated. Multiplying the unit Reynolds number by the chord length at each section results in the Reynolds number. Like most CFD codes, FLO_MG has stability problems when the Mach number is too low, as is the case for most sections. Considering the fact that compressibility effects do not come into play until Mach ~ 0.3, it is safe to assume that the results will still be satisfactory if the Mach number is increased to computationally acceptable values. So Mach = 0.106 (the value for the airfoil section at $\xi = 0.6$) for airfoil sections at $\xi = 0.1$ to $\xi = 0.5$ was used to permit stable calculations and keep correct values of the respective Reynolds number.

Besides the dimensionless geometrical coordinates, the Mach number, and the Reynolds number, additional information was needed to create the input file, such as the angle of attack, which is –4, -2, 0, 2, 4, 6, 8, and the specified number of grid points in computational domain, which is 321*64.

(3) Mesh

The mesh is the intermediate output of FLO_MG. [2] A good mesh is necessary to guarantee meaningful numerical results. All the input information should be written into the FLO_MG requested input format. There are several shapes for grids around two-dimensional bodies: C-grids, H-grids, and O-grids etc. C-grids work best when the airfoils have sharp trailing edges, and O-grids are best for airfoils having blunt, rounded trailing edges. Unfortunately, the grid generator of FLO_MG is not designed to handle airfoils like the ones in the project (O-grids), i.e., having a concave lower surface and a blunt trailing edge. It was designed to generate C-grids only. So, to get a reasonable mesh, either a different grid generator had to be used, or the shape of the trailing edge had to be altered. The latter method was chosen in this computational project to get rid of the generation problem: a few points around the trailing edge on both sides were removed to sharpen the trailing edges, while all other parameters in the input files remained the same. The corresponding mesh with 321*65 grid points was very good. Figures 4.01 to 4.08 are the mesh plots of each cross section (from ξ =0.2 to ξ =0.9).

(4) The blade section lift coefficient and the blade section drag coefficient

All flow solvers, including FLO_MG, work on the principle that the relevant equations, usually some form of the Navier-Stokes or Euler equations, are iterated until a satisfactory solution is obtained. For all the project cases-- depending on the Mach number, Reynolds number, and angle of attack -- one would want the solution to run long enough so that the flow around the airfoil is reasonably stable, i.e., it doesn't change with time (time, of course, being represented by number of iterations), or the changes are periodic. One program of FLO_MG named exflomg is used to extract the convergence history for C_l and C_d. [2,3] In the first instance, one would expect a plot of, say, lift coefficient (C_l), to look like the ones in Figure 5.01. Note from the first plot that the C_l fluctuates initially, but eventually reaches a value that remains constant regardless of the number of additional iterations. This solution is converged, and it represents a steady state for the flow (the discontinuous breaks in the convergence plot represent the places where the density of the grid points was increased. The number of iterations at which this occurs is specified in the input file for program). The solution in Figure 5.02 is not as steady as Figure 5.01, but it is acceptable. In the second instance, the flow may become unsteady, i.e., it is time dependent. In this project, the prime reason for this is that the flow separated from the surface of the airfoil. This behavior is manifested as oscillations in the convergence histories of parameters like C_l and C_d, as can be seen in Figure 5.03 and Figure 5.04. Some times the amplitude of the oscillations remains constant, and sometimes it increases, as is the case in the Figure 5.04. If the flow is separated, then the value for the force coefficients changes with time. If the solution doesn't change with time, then the output values of C_l and C_d are the correct values, since these are the ones corresponding to the last iteration. If the solution changes with time, then the output values do not necessarily represent the "true" values. In this case, the average of the last 150 values for C_l and C_d found in the convergence history are used to obtain a average value steady-stats, which is a more appropriate representation of the true coefficient. Tables 1.01 to 1.10 are C_l and C_d vs. angle of attack at different cross sections (using the same values at ξ =0.9 for the values at ξ =0.96 and ξ =1). Figures 6.01 to 6.10 are the relevant plots respectively (using the same values at ξ =0.9 for the values at ξ =0.96 and ξ =1). Figures 7.01 to 7.10 are the relevant plots respectively (using the same values at ξ =0.9 for the values at ξ =0.96 and ξ =1).

B. Calculation on Propeller Design Analysis Code

(1) The Input

The input should also be written into the code specified format. There are two input files for the Propeller Design Analysis Code. [4] The first one is a common input file, which is the basic input for all test cases. It includes all the C_l and C_d gotten from FLO_MG at normalized span locations, the number of blades (which is 2); blade radius (which is 4.25ft); the number of specified angles of attack (which is 7), and the specified angle of attack (which are –4, -2, 0, 2, 4, 6, 8), etc. These parameters keep constant for all test cases. The second input file is a special input file, which includes the propeller design RPM, design forward velocity, the dynamic pressure, and the relaxation parameter that can be played to ensure convergence. These parameters are case dependent. There are two primary sets of computational runs. In the first group, the Propeller RPM was specified as 400, with the design speed ranging from 8.69 knots to 43.45 knots. In the second group, the design velocity was specified at 34.76 knots, with the design RPM ranging from 325 to 2000.

(2) The Output

The thrust coefficient, C_T, power coefficient, C_p, and the efficiency, η, are the final output of this project. Table 2.01 supplies the calculated advance ratio J, the C_T, C_p, and η from the propeller code output with specified RPM equal to 400. Table 2.02 supplies the calculated advance ratio, J, the C_T, C_p, and η from the code output with specified velocity equal to 34.76. Figure 8.01 shows C_T vs. J of the two parametric groups. Figure 8.02 shows C_p vs. J of the two groups. Figure 8.03 shows η vs. J for the two groups of occasions.

Analysis of the result

Table 3.01 is a comparison of C_T between experiment and computation. Table 3.02 is a comparison of C_p between experiment and computation. Table 3.03 is a comparison on η between experiment and computation. The Figures 9.01 to 9.03 are the relevant plots for the comparison. From the comparison, it can be seen that from J=0.6 to J=1.15, the computed results complied with the experimental results very well. In fact, from J=0.6 to J=1.15 (the stalled advance ratio of experiment), the computational values are a little higher than the experimental ones. There are obvious differences when J is below 0.6. This is mainly because of the unreliability of the computational results when J is too low (The angle of attack in the output is far outside the specified range, which is from –4d to 8d). In the experiment, stall occurred at J=1.15, while in the computation the stall occurred at J=1.29. In the other words, the computational η values still increased from j=1.15 to j=1.29, but the experimental values decreased. In the experiment, max efficiency is 0.87 at j=1.15 (in the computational result, at J=1.15, η=0.894); In the computational result, the maximum efficiency was 0.93 at j=1.29. According to the empirical expectation, the stall advance ratio should not be as high as 1.29 in the computation. The main reason of the computational result may be on the sharpen of the trailing edge in order to generate C-grids for FLO_MG. This alteration brought inaccuracy on the lift coefficient and drag coefficient, which changed the final stall position. The relaxation coefficient in the input file of the Propeller code may be another factor to influence the stall. The proper relaxation coefficient should be given other than 10 to all the cases. Anyway, the fault on the difference is because of some approximation in the computation. So it can be concluded that the experimental results from Langley is quite reliable, and the Wright " Bent end" propeller does have a very high propulsive efficiency that is as good as or better than modern propeller.

Acknowledgements

The author would like to acknowledge the support from the Eagle Aeronautics, Inc, and the Aerospace Engineering Department, Old Dominion University.

References

1. S. J. Miley, R. L. Ash, K. W. Hyde, D. Landman, A. K. Sparks., *"Propeller Performance Test of Wright Brothers' 'Bend End' Propellers"*, Journal of Aircraft, Vol. 39, No. 2. March—April 2002
2. R.C. Swanson., *"Artificial Dissipation and Central Difference Schemes For the Euler and Navier – Stokes Equations"* AIAA-87-1107, AIAA 8th computational Fluid Conference, June 1987
3. Percy J Bobbitt, Anna. Tinetti., *"Global Aircraft Corporation Quasi-constant Speed fixed-Pitched Composite Propeller"* Project No. 94-1-01.04-2800, May 1996
4. C. N. Adkins, R. H. Liebeck., *"Design of Optimum Propellers"* AIAA-83-0190, AIAA 21st Aerospace Sciences Meeting, January 1983

Appendix: the important figures and tables

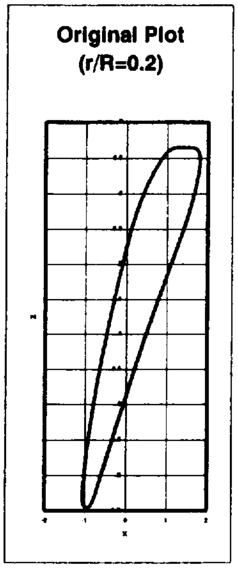

Figure 1.01 Blade contour at ξ=20%

(Area 4.605, Perimeter 12.238, x_{le} =1.742, z_{le} =6.615, x_{te} =-0.997, z_{te} =1.554, c=5.7546, ϕ=61.5779d)

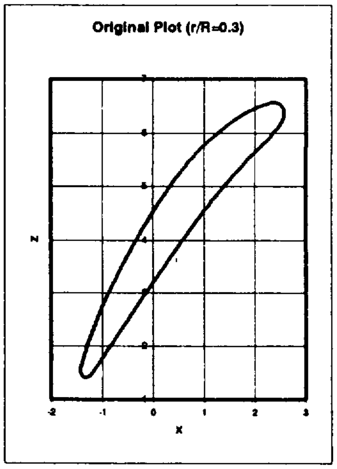

Figure 1.02 Blade contour at ξ=30%

(Area 4.184, Perimeter 13.367, x_{le} =2.488,z_{le} = 6.524 , x_{te} =-1.377, z_{te} =1.427 , c= 6.3967, ϕ= 52.8274d)

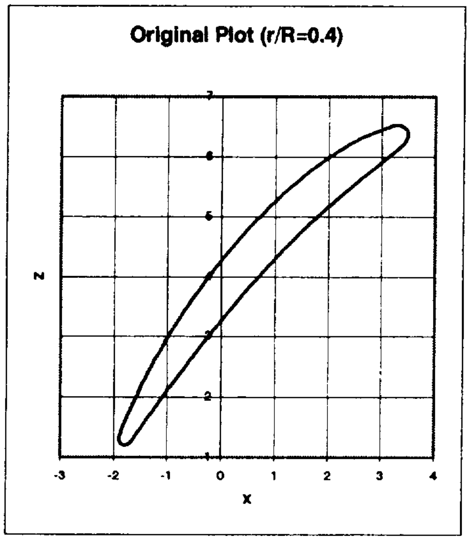

Figure 1.03 Blade contour at ξ=40%

(Area =4.330, Perimeter = 15.489, x_{le} =3.441, z_{le} =6.483, x_{te} =-1.852, z_{te} =1.223, c= 7.4621, ϕ= 44.8208d)

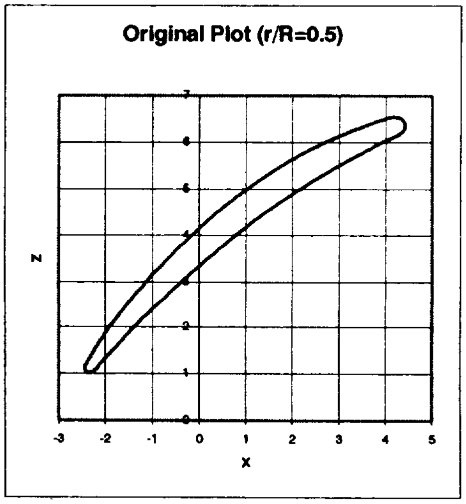

Figure 1.04 Blade contour at ξ=50%

(Area =4.647, Perimeter = 18.004, x_{le} =4.39, z_{le} =6.458, x_{te} =-2.41, z_{te} =1.036, c= 8.6970, ϕ= 38.5672d)

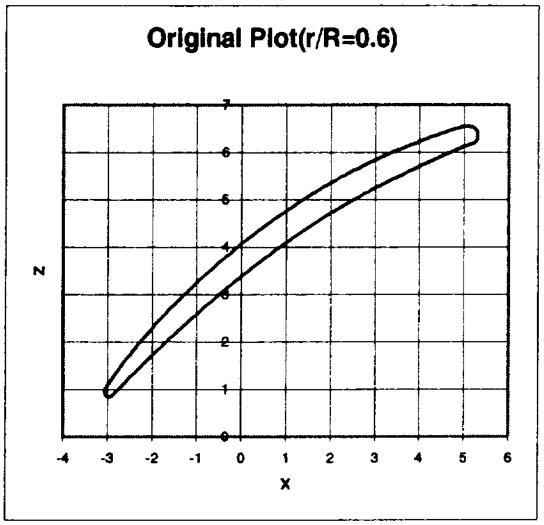

Figure 1.05 Blade contour at ξ=60%

(Area =4.895, Perimeter = 20.630, x_{le} =5.265, z_{le} =6.476, x_{te} =-3.04, z_{te} =0.891, c= 10.0083, ϕ= 33.9203d)

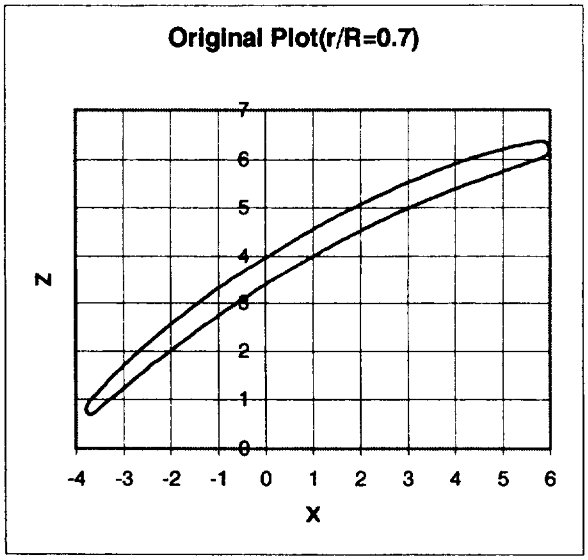

Figure 1.06 Blade contour at ξ=70%

(Area =4.985, Perimeter = 22.973, x_{le} =5.957, z_{le} =6.288, x_{te} =-3.783, z_{te} =0.746, c= 11.2063, ϕ=29.6396d)

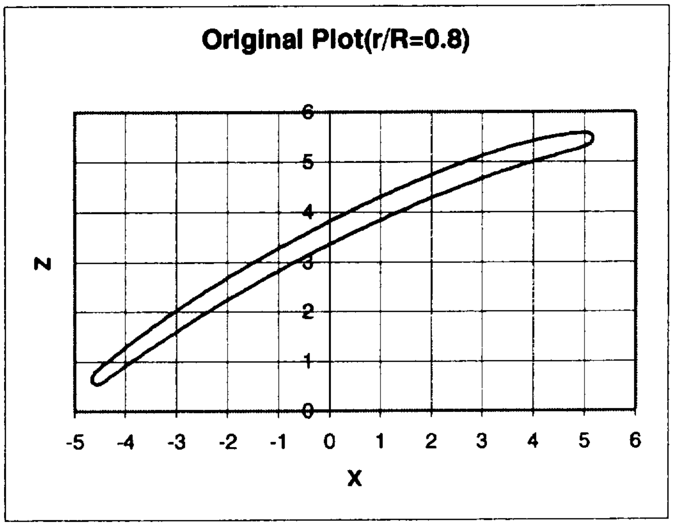

Figure 1.07 Blade contour at ξ=80%

(Area =4.170, Perimeter = 22.397, x_{le} =5.157, z_{le} =5.501, x_{te} =-4.657, z_{te} =0.606, c= 10.9670, ϕ=26.5090d)

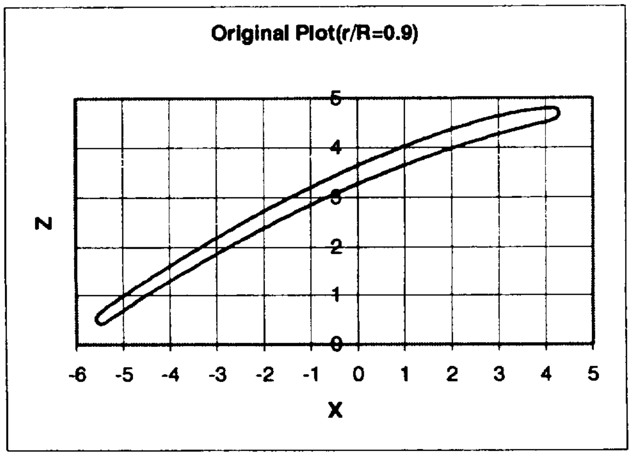

Figure 1.08 Blade contour at ξ=90%

(Area =3.350, Perimeter = 21.834, x_{le} =4.28, z_{le} =4.721, x_{te} =-5.564, z_{te} =0.482, c= 10.7179, ϕ= 23.2976)

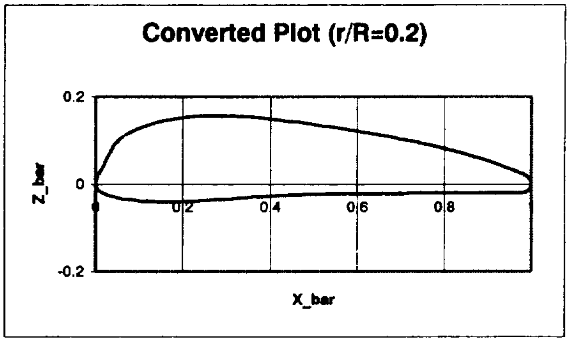

Figure 2.01 Dimensionless, reoriented blade at ξ=20%

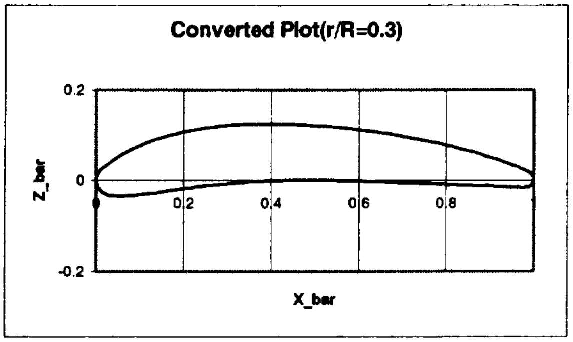

Figure 2.02 Dimensionless, reoriented blade at ξ=30%

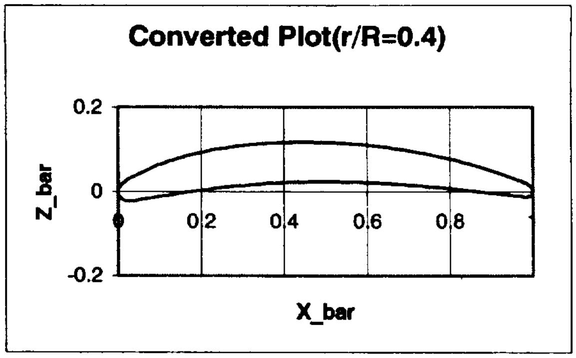

Figure 2.03 Dimensionless, reoriented blade at ξ=40%

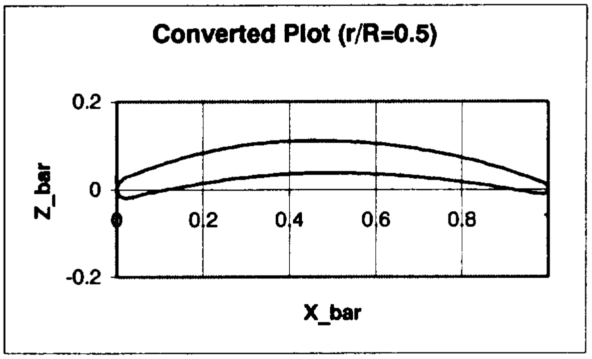

Figure 2.04 Dimensionless, reoriented blade at ξ=50%

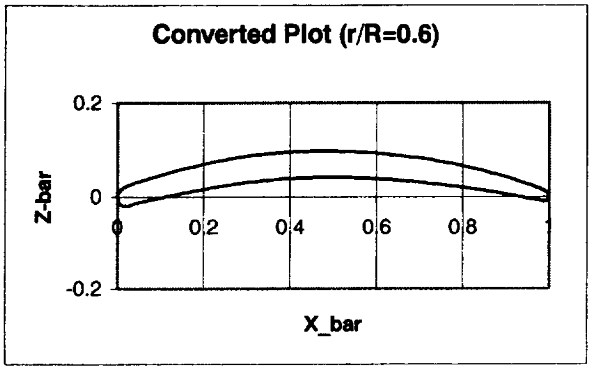

Figure 2.05 Dimensionless, reoriented blade at ξ=60%

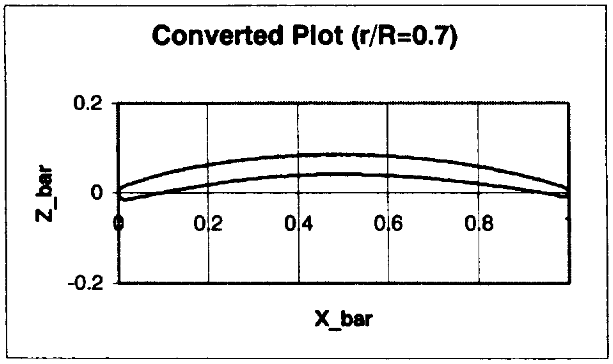

Figure 2.06 Dimensionless, reoriented blade at ξ=70%

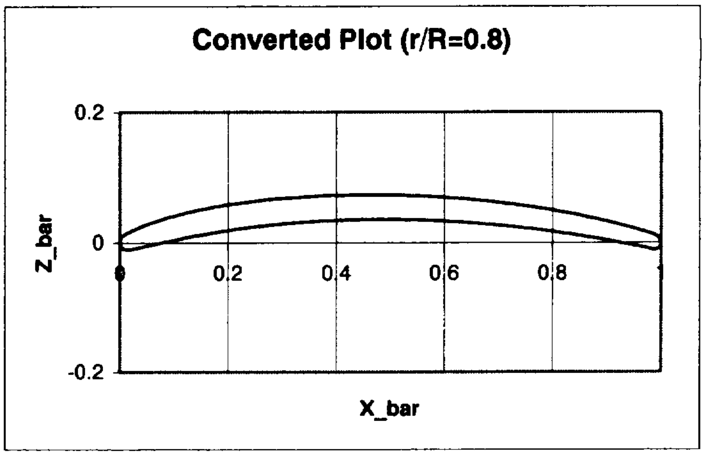

Figure 2.07 Dimensionless, reoriented blade at ξ=80%

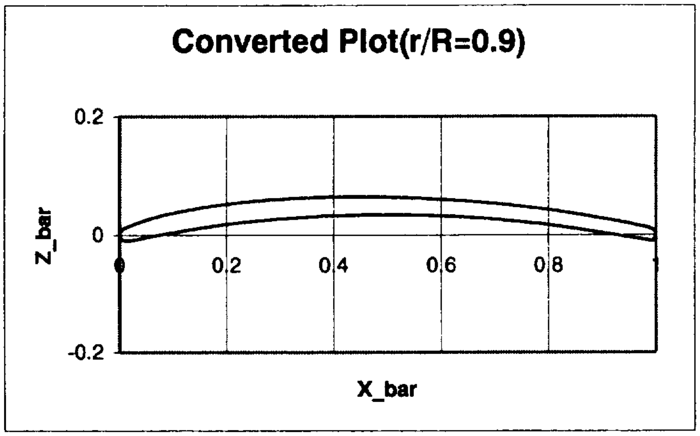

Figure 2.08 Dimensionless, reoriented blade at ξ=90%

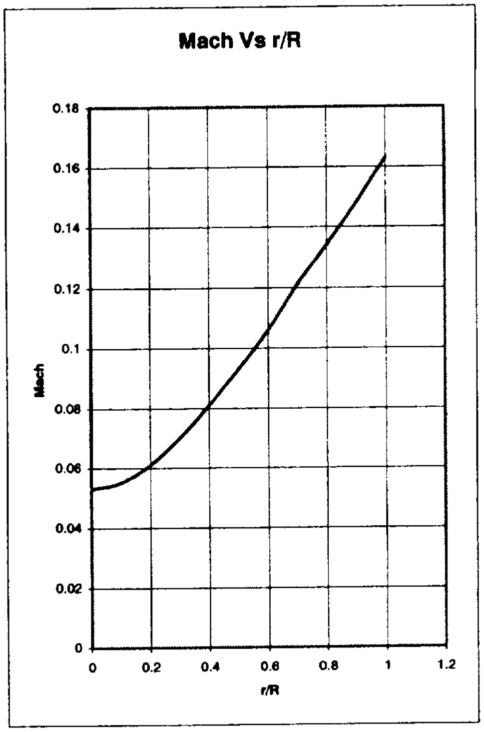

Figure 3.01 Variation of Mach number with blade location; Input for FLO_MG

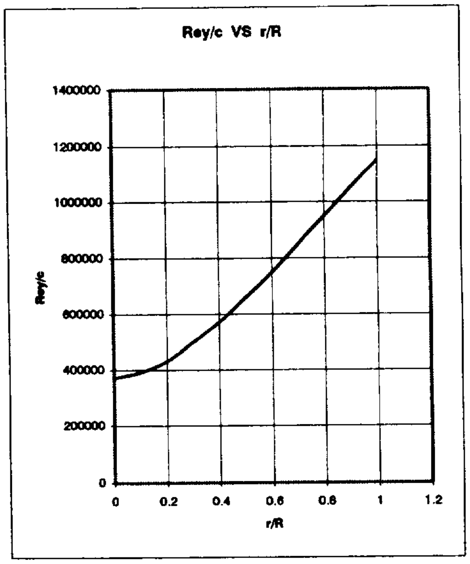

Figure 3.02 Unit Reynolds number as a function of blade location

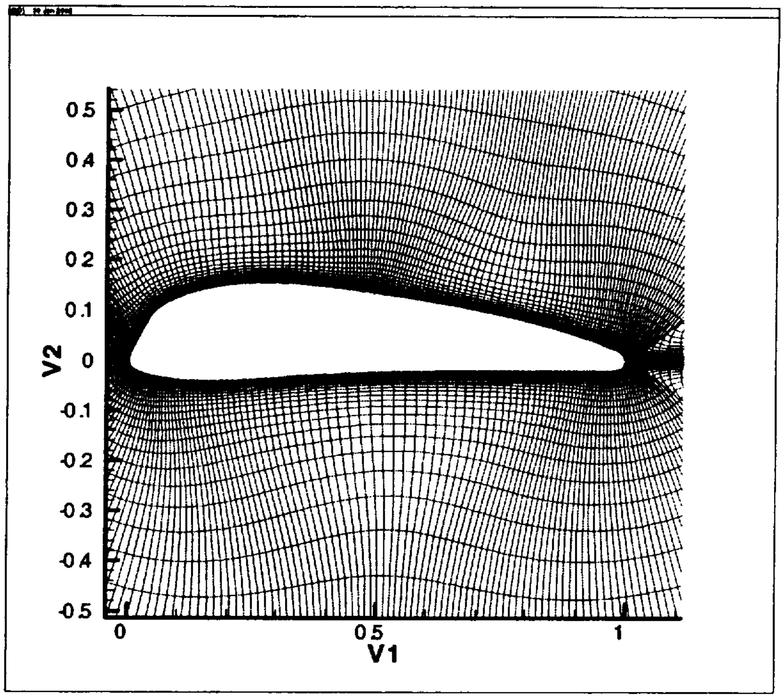

Figure 4.01 Computational grid for ξ=20%

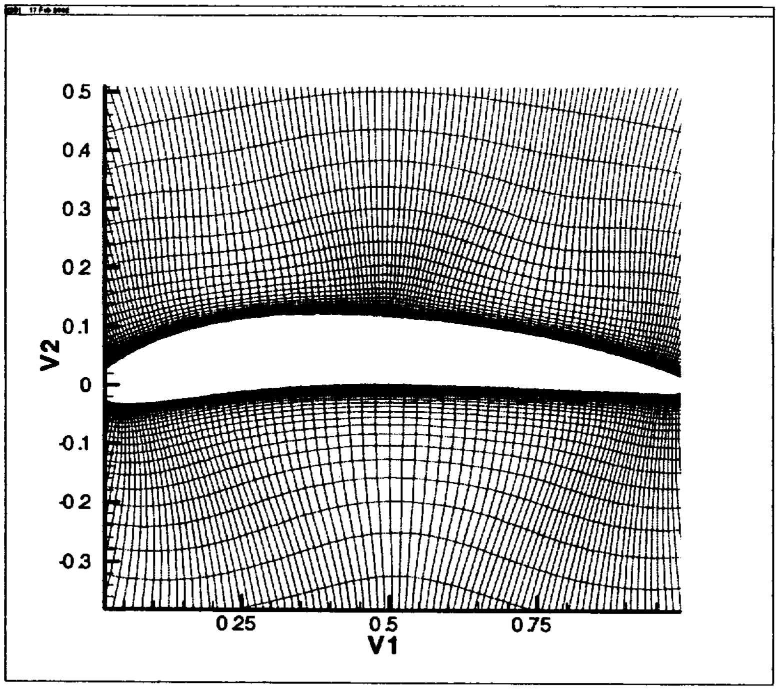

Figure 4.02 Computational grid for ξ=30%

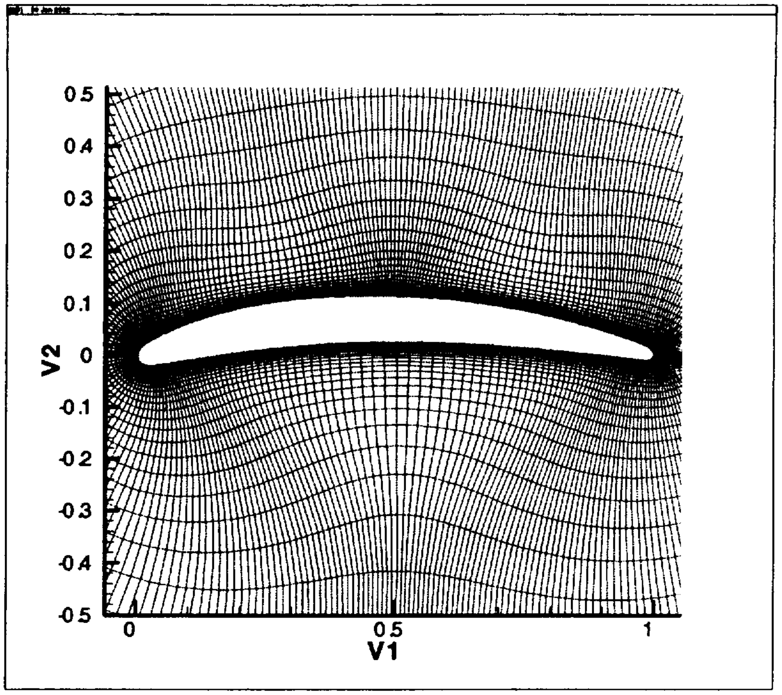

Figure 4.03 Computational grid for ξ=40%

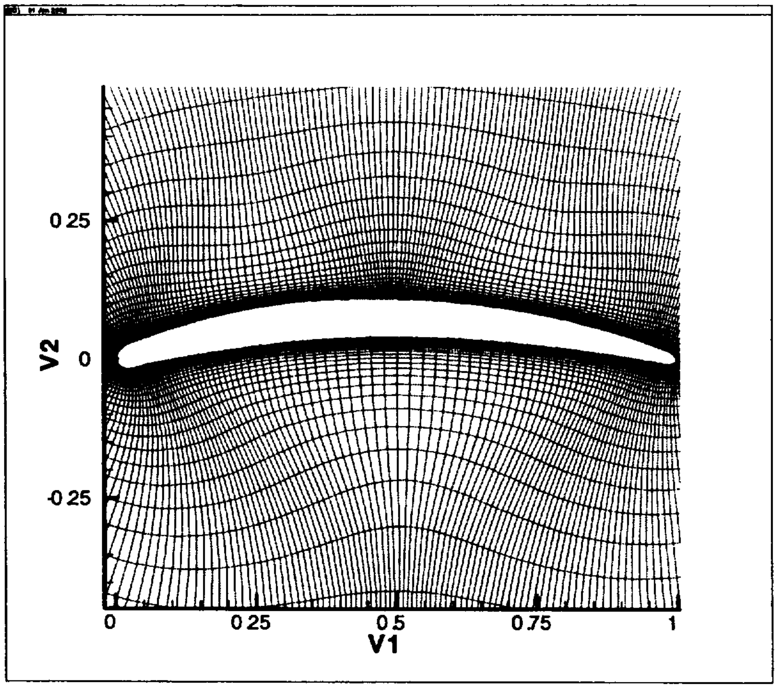

Figure 4.04 Computational grid for ξ=50%

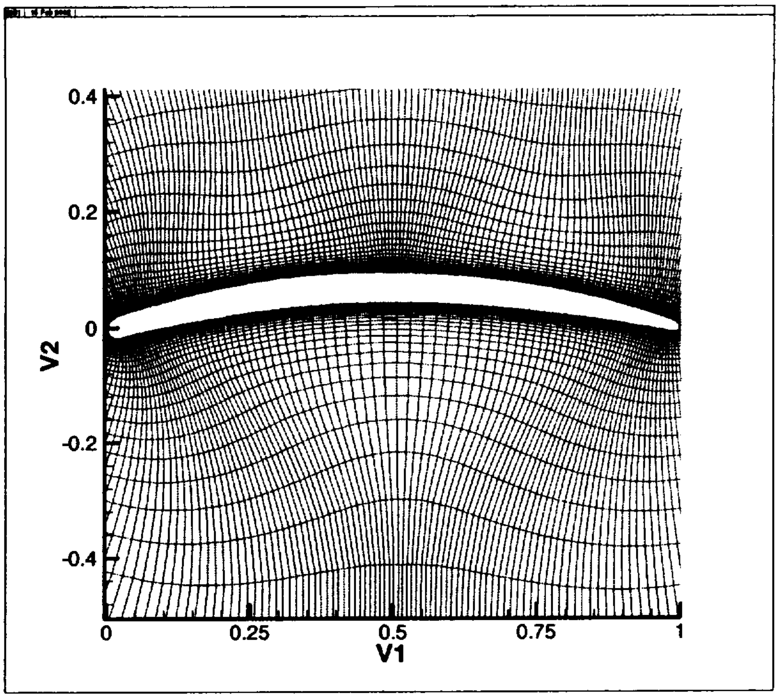

Figure 4.05 Computational grid for ξ=60%

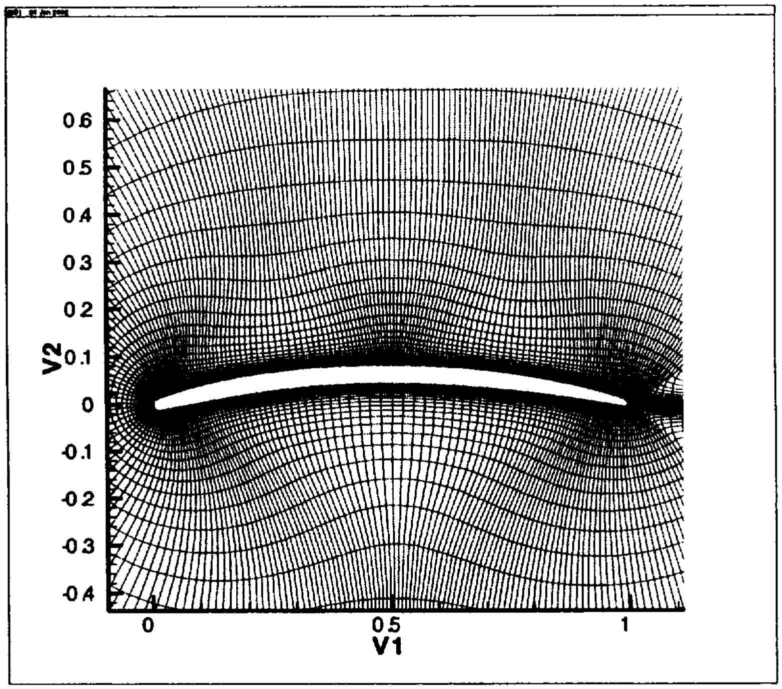

Figure 4.06 Computational grid for ξ=70%

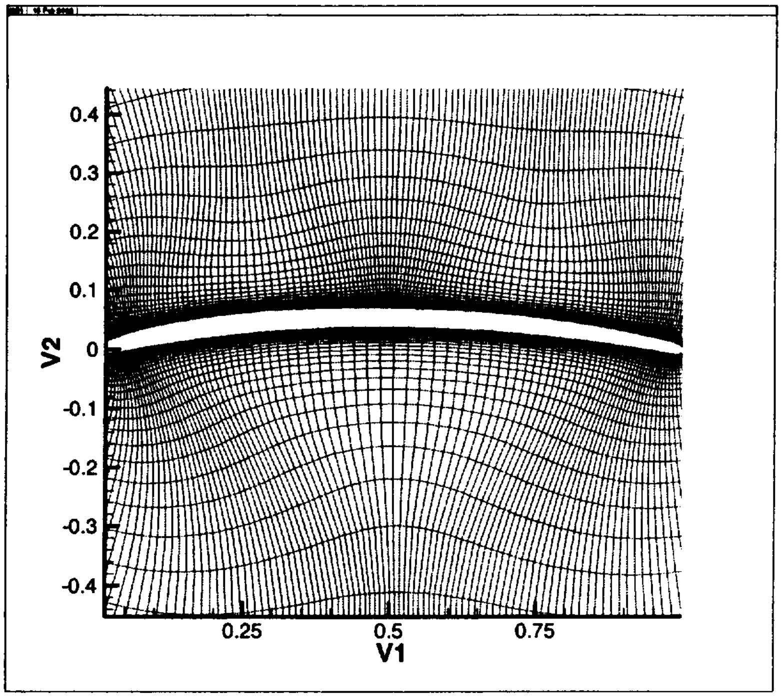

Figure 4.07 Computational grid for ξ=80%

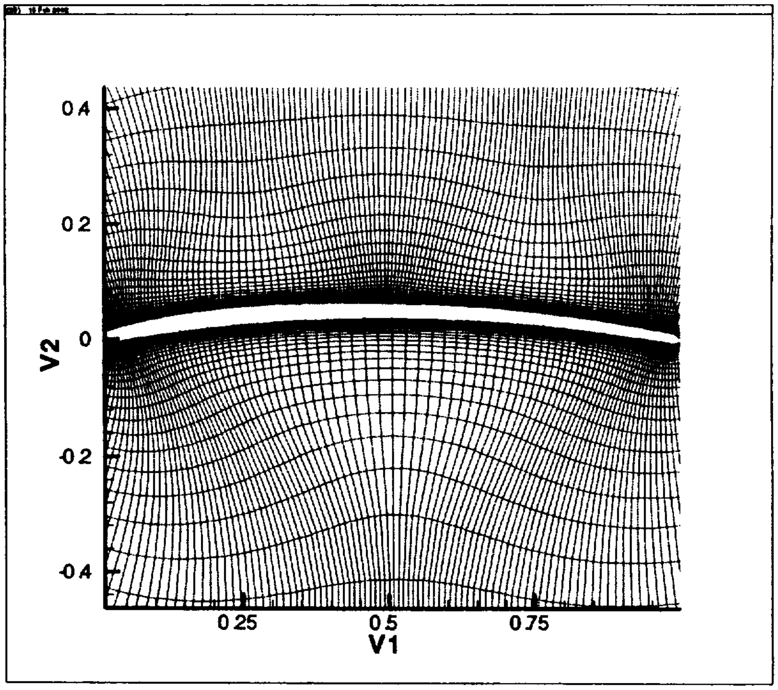

Figure 4.08 Computational grid for ξ=90%

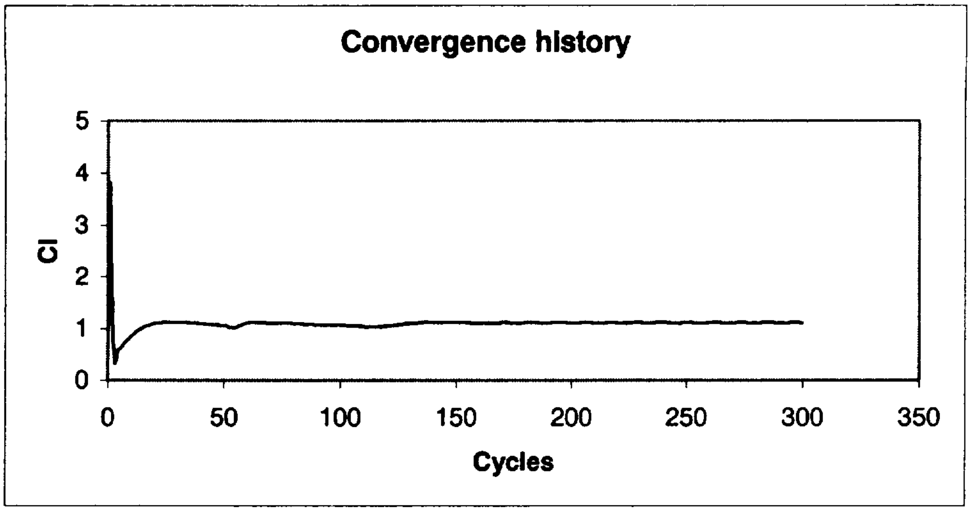

Figure 5.01 Representative C_l convergence history for a well behaved convergence

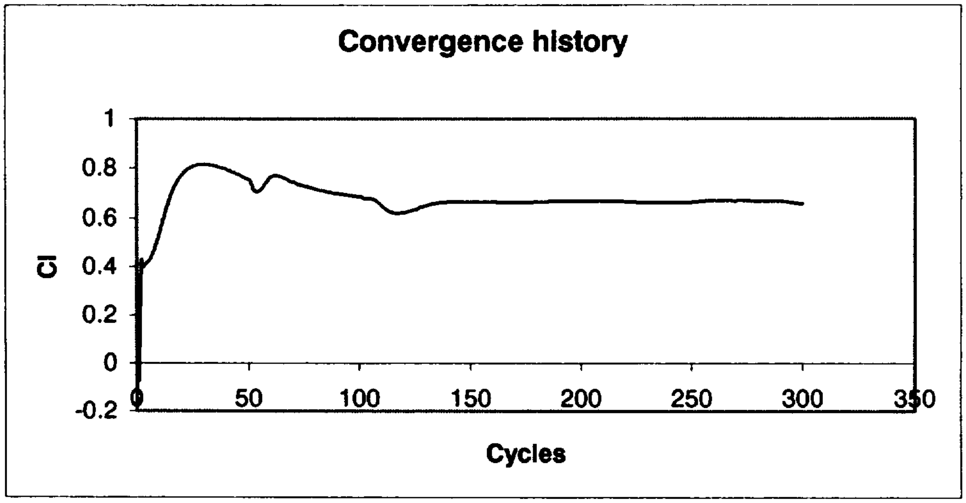

Figure 5.02 Representative C_l convergence history for a weakly stable convergence

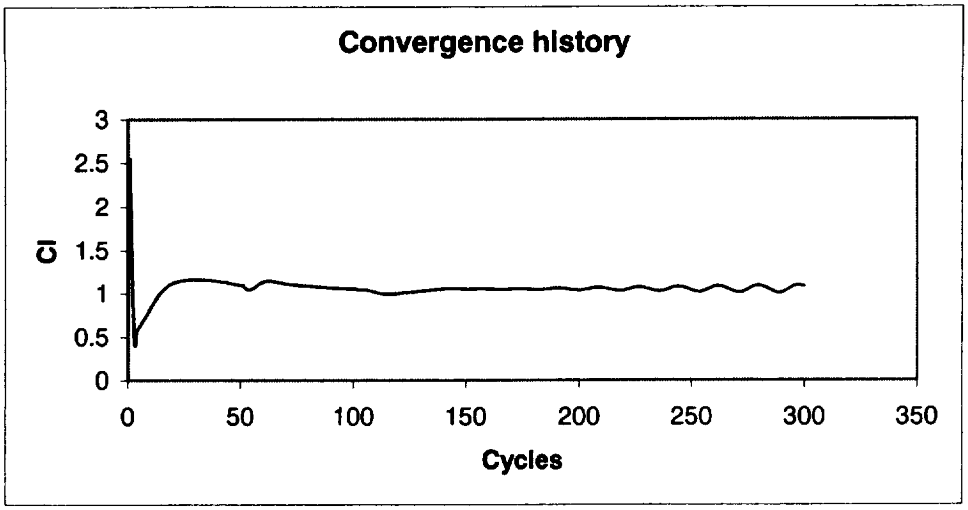

Figure 5.03 Representative C_l convergence history for an unstable convergence, showing a growing oscillation

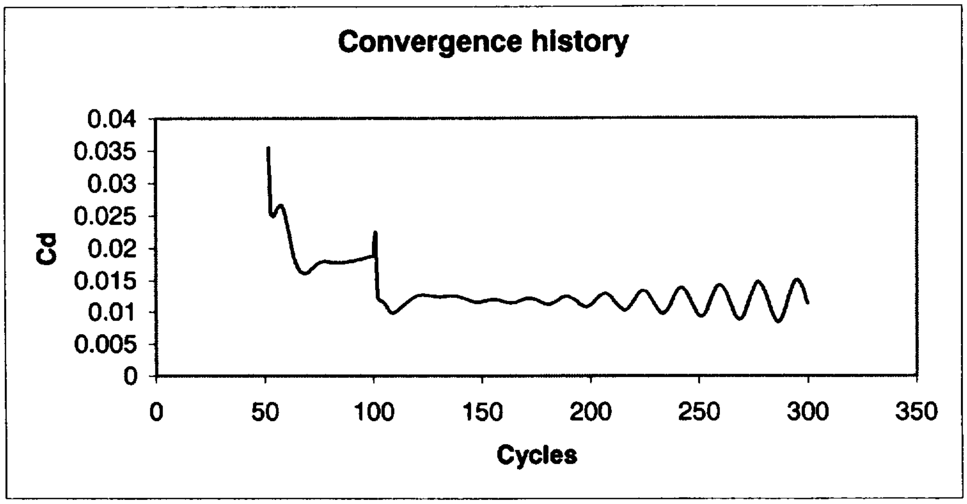

Figure 5.04 Representative C_d convergence history for an unstable convergence

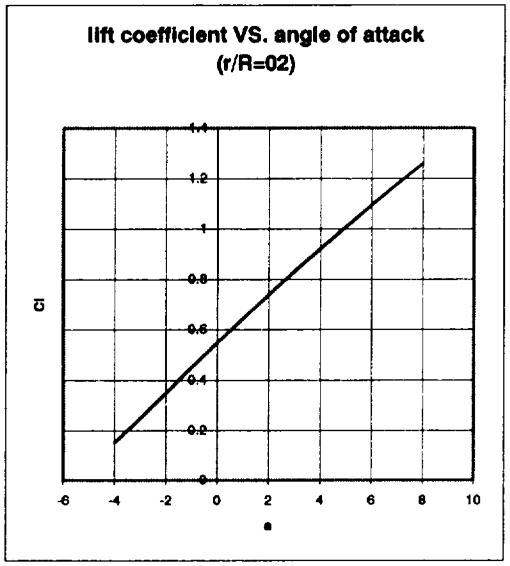

Figure 6.01 Lift coefficient VS. angle of attack at ξ=20%

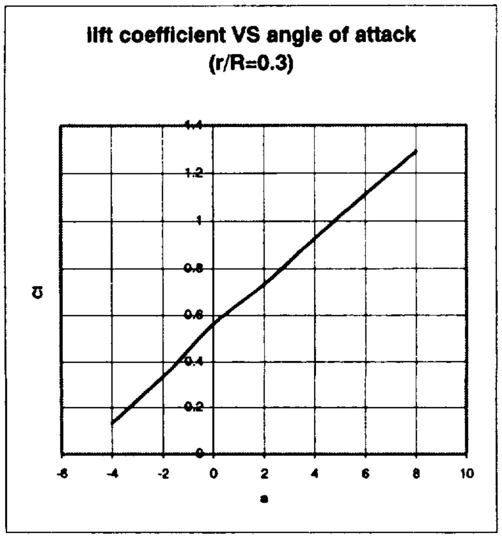

Figure 6.02 Lift coefficient VS. angle of attack at ξ=30%

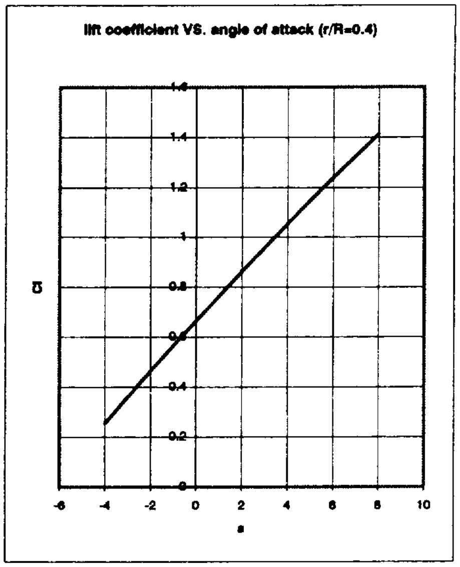

Figure 6.03 Lift coefficient VS. angle of attack at ξ=40%

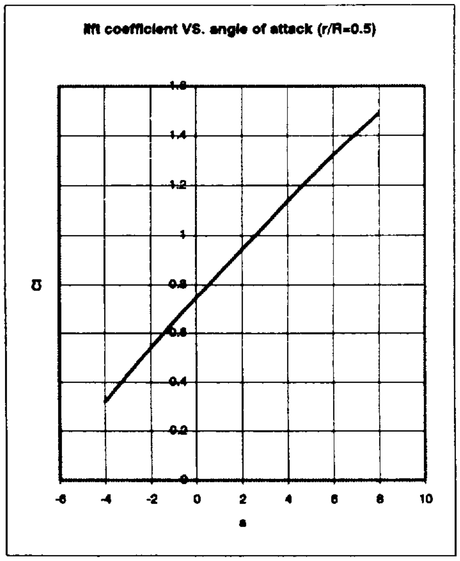

Figure 6.04 Lift coefficient VS. angle of attack at ξ=50%

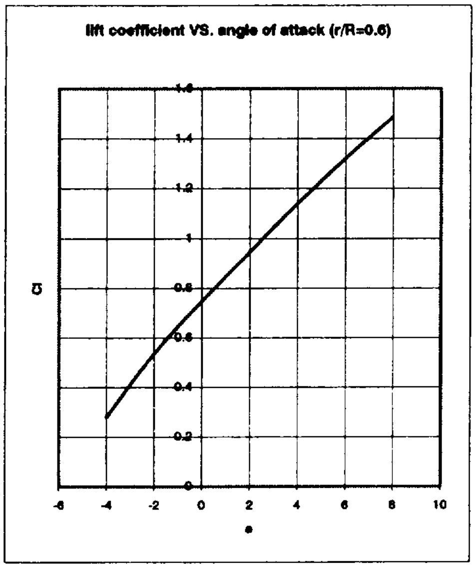

Figure 6.05 Lift coefficient VS. angle of attack at ξ=60%

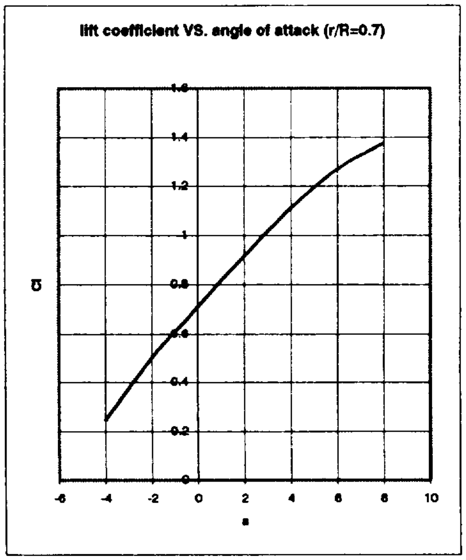

Figure 6.06 Lift coefficient VS. angle of attack at ξ=70%

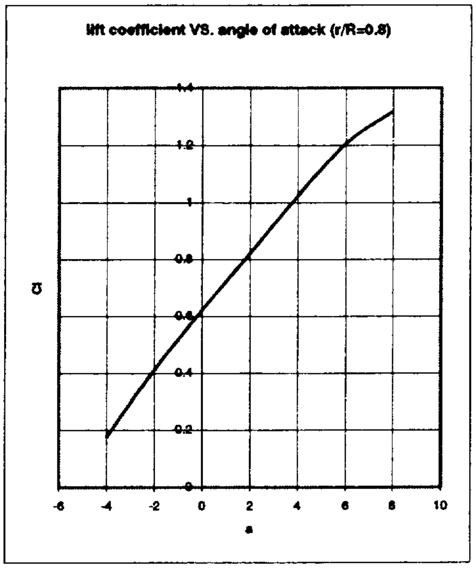

Figure 6.07 Lift coefficient VS. angle of attack at ξ=80%

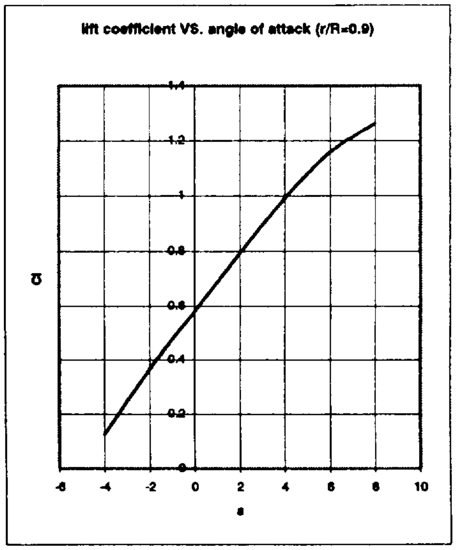

Figure 6.08 Lift coefficient VS. angle of attack at ξ=90%

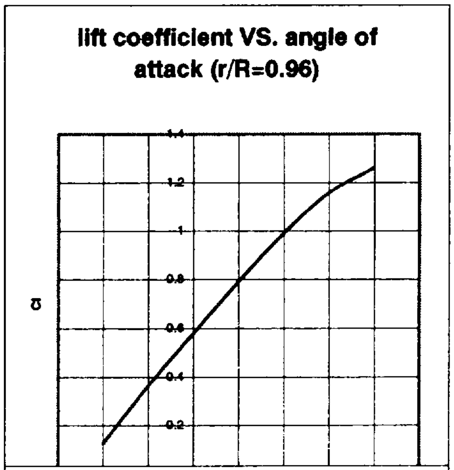

Figure 6.09 Lift coefficient VS. angle of attack at ξ=96% (Same as ξ=90%)

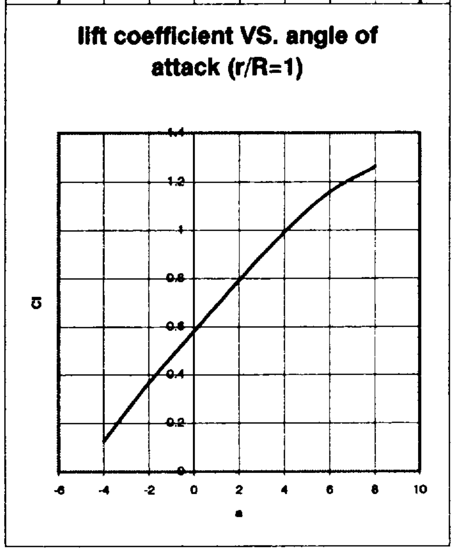

Figure 6.10 Lift coefficient VS. angle of attack at ξ=100% (Same as ξ=90%)

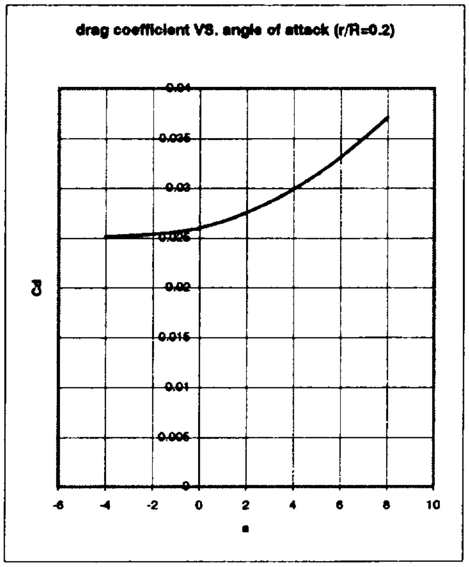

Figure 7.01 Drag coefficient VS. angle of attack at ξ=20%

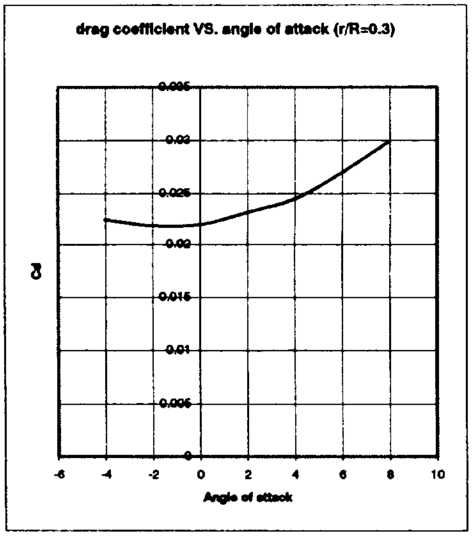

Figure 7.02 Drag coefficient VS. angle of attack at ξ=30%

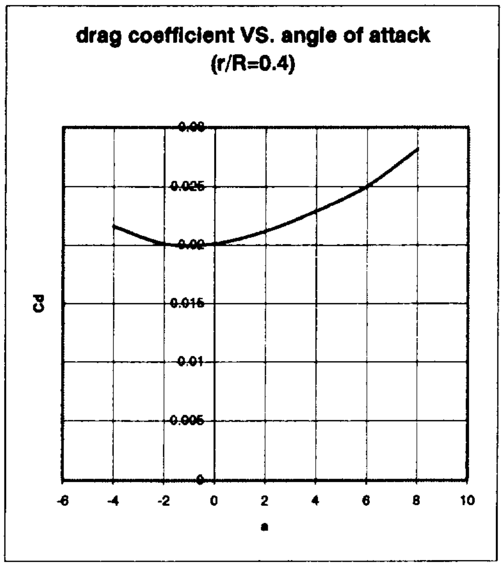

Figure 7.03 Drag coefficient VS. angle of attack at ξ=40%

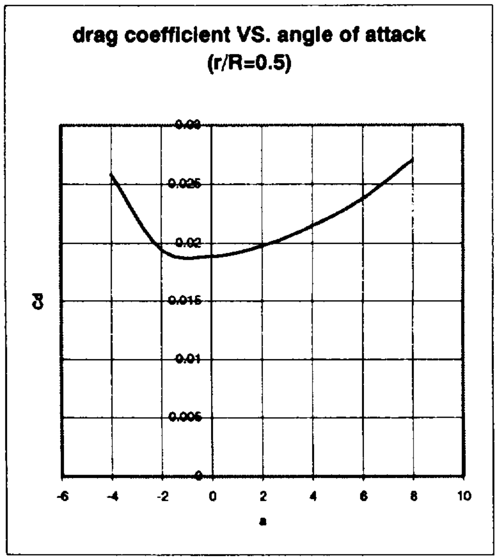

Figure 7.04 Drag coefficient VS. angle of attack at ξ=50%

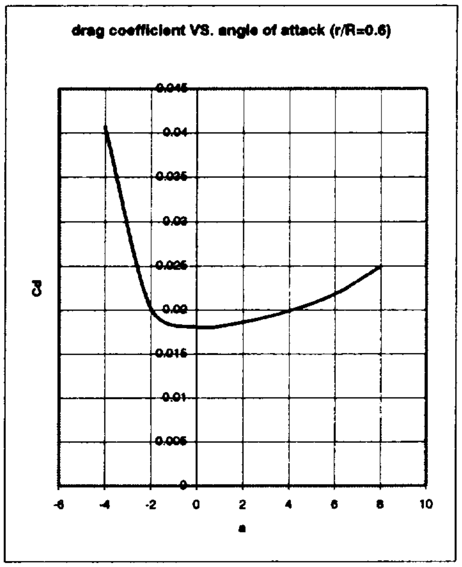

Figure 7.05 Drag coefficient VS. angle of attack at ξ=60%

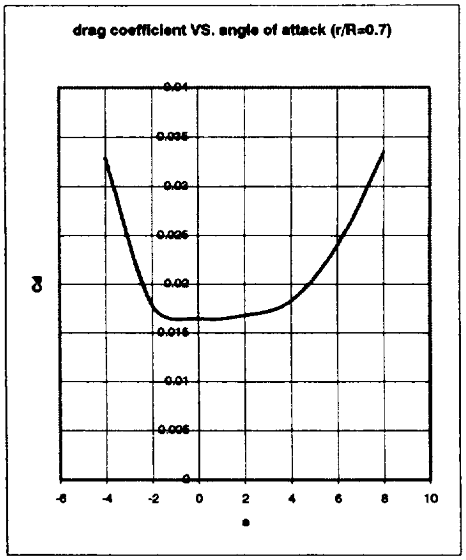

Figure 7.06 Drag coefficient VS. angle of attack at ξ=70%

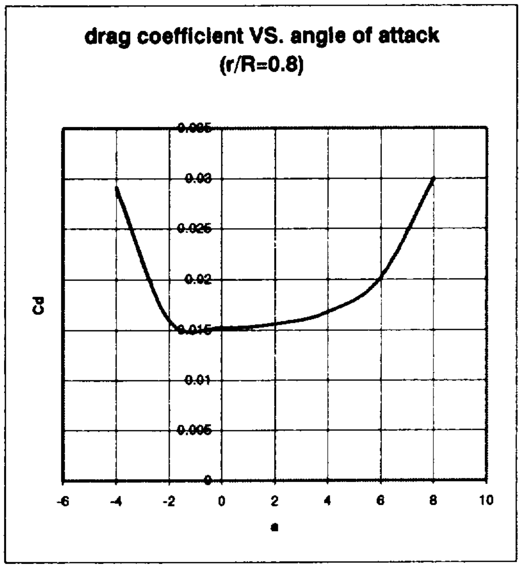

Figure 7.07 Drag coefficient VS. angle of attack at ξ=80%

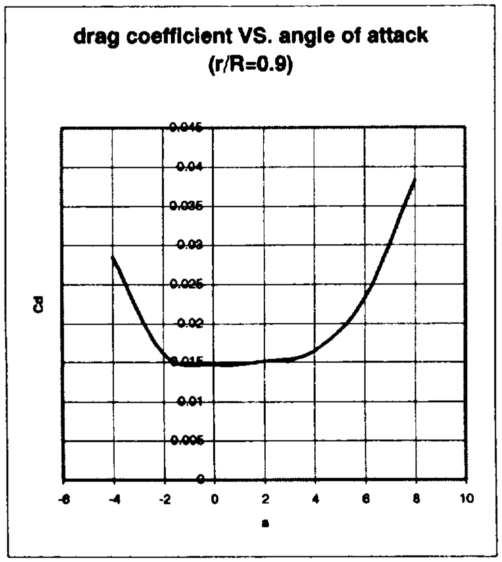

Figure 7.08 Drag coefficient VS. angle of attack at ξ=90%

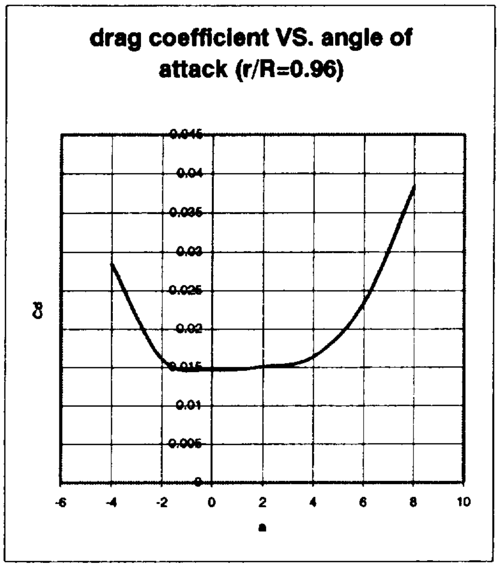

Figure 7.09 Drag coefficient VS. angle of attack at ξ=96%

(Same as ξ=90%)

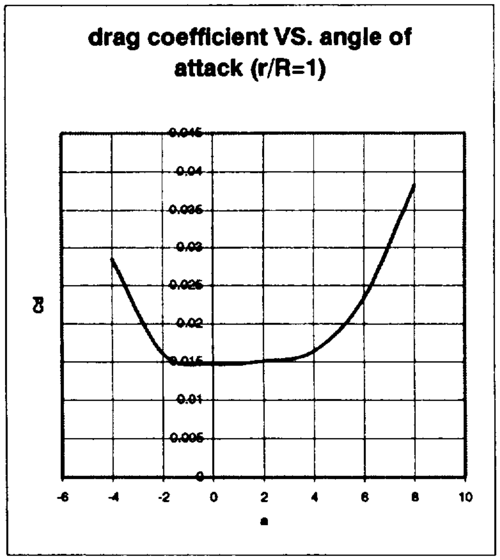

Figure 7.10 Drag coefficient VS. angle of attack at ξ=100%

(Same as ξ=90%)

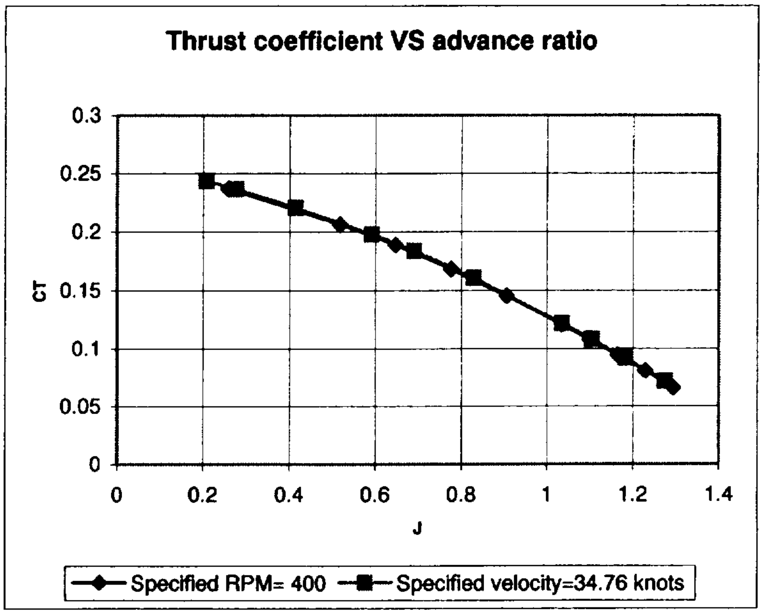

Figure 8.01 Comparison of fixed rotational speed and fixed flow-speed CFD predictions of thrust coefficient VS. advance ratio

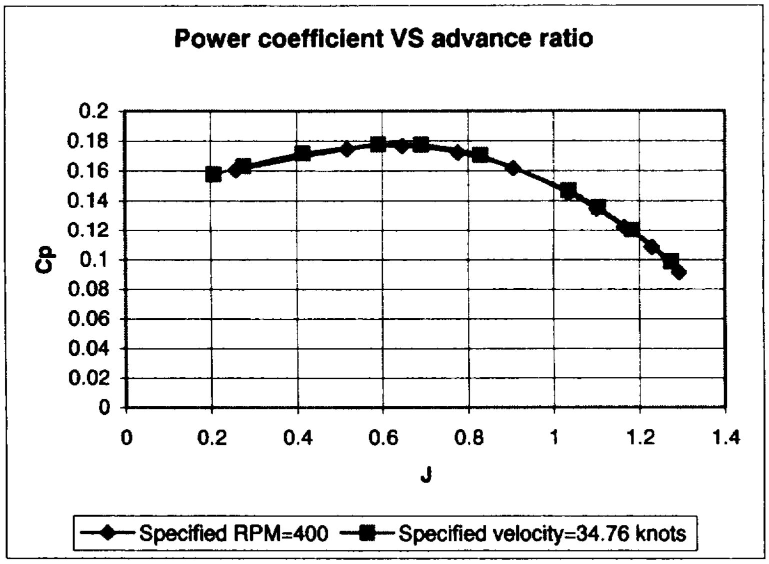

Figure 8.02 Comparison of fixed rotational speed and fixed flow-speed CFD predictions of power coefficient VS. advance ratio

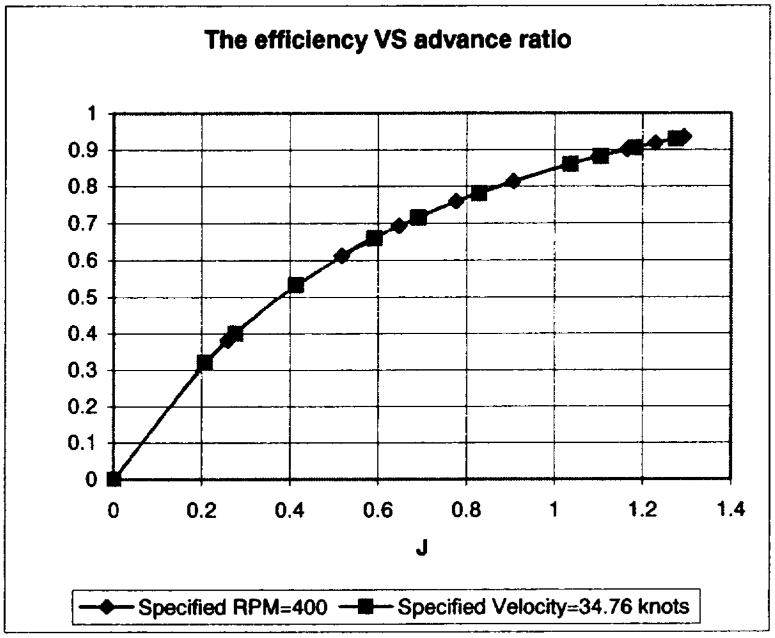

Figure 8.03 Comparison of fixed rotational speed and fixed flow-speed CFD predictions of efficiency VS. advance ratio

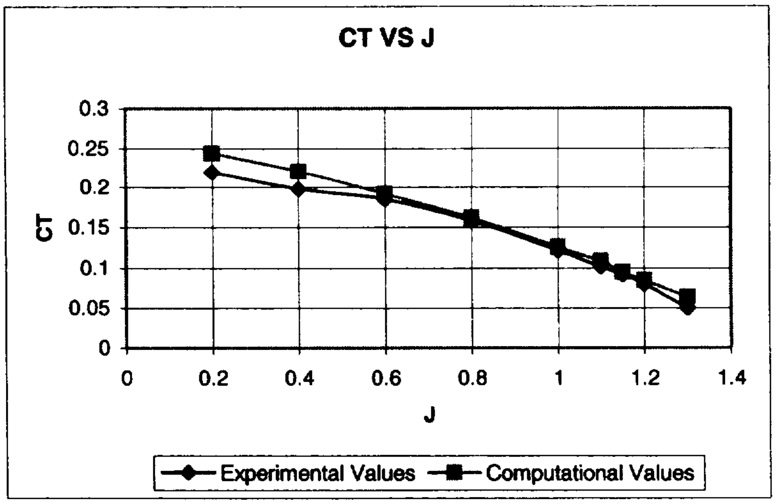

Figure 9.01 Comparison between numerical predictions and experimental measurements of thrust coefficient VS. advance ratio

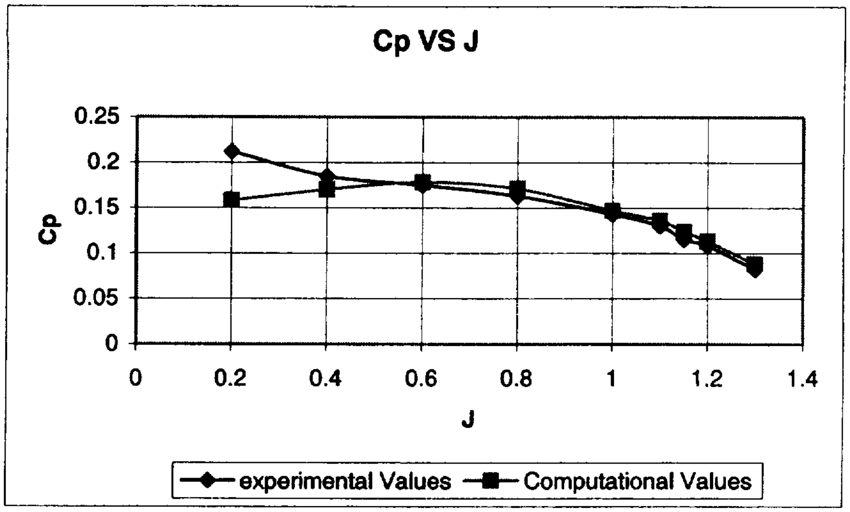

Figure 9.02 Comparison between numerical predictions and experimental measurements of power coefficient VS. advance ratio

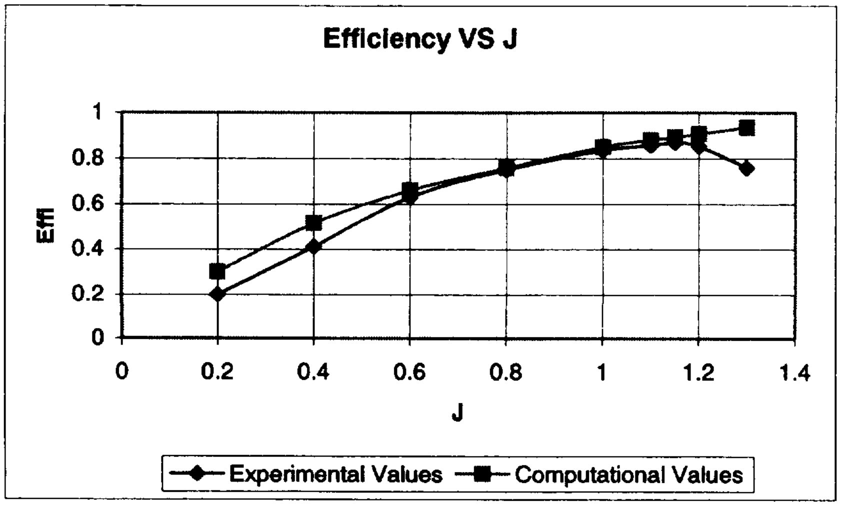

Figure 9.03 Comparison between numerical predictions and experimental measurements of efficiency VS. advance ratio

a	C_l	C_d
-4.00E+00	1.53E-01	2.51E-02
-2.00E+00	3.50E-01	2.54E-02
0.00E+00	5.49E-01	2.60E-02
2.00E+00	7.38E-01	2.76E-02
4.00E+00	9.22E-01	2.99E-02
6.00E+00	1.10E+00	3.31E-02
8.00E+00	1.26E+00	3.72E-02

Table 1.01 Lift coefficient and Drag coefficient VS. angle of attack at ξ=20%

(Mach=0.106, Rey= 206000)

a	C_l	C_d
-4.00E+00	1.33E-01	2.25E-02
-2.00E+00	3.34E-01	2.19E-02
0.00E+00	5.63E-01	2.20E-02
2.00E+00	7.33E-01	2.32E-02
4.00E+00	9.28E-01	2.45E-02
6.00E+00	1.11E+00	2.70E-02
8.00E+00	1.29E+00	2.99E-02

Table 1.02 Lift coefficient and Drag coefficient VS. angle of attack at ξ=30%

(Mach=0.106, Rey= 267000)

a	C_l	C_d
-4.00E+00	2.55E-01	2.16E-02
-2.00E+00	4.64E-01	2.01E-02
0.00E+00	6.65E-01	2.01E-02
2.00E+00	8.62E-01	2.12E-02
4.00E+00	1.05E+00	2.29E-02
6.00E+00	1.24E+00	2.50E-02
8.00E+00	1.41E+00	2.81E-02

Table 1.03 Lift coefficient and Drag coefficient VS. angle of attack at ξ=40%

(Mach=0.106, Rey=354000)

a	C_l	C_d
-4.00E+00	3.20E-01	2.58E-02
-2.00E+00	5.40E-01	1.95E-02
0.00E+00	7.46E-01	1.89E-02
2.00E+00	9.44E-01	1.98E-02
4.00E+00	1.14E+00	2.15E-02
6.00E+00	1.32E+00	2.38E-02
8.00E+00	1.49E+00	2.70E-02

Table 1.04 Lift coefficient and Drag coefficient VS. angle of attack at ξ=50%

(Mach=0.106, Rey= 478000)

a	C_l	C_d
-4.00E+00	2.79E-01	4.07E-02
-2.00E+00	5.35E-01	2.02E-02
0.00E+00	7.49E-01	1.80E-02
2.00E+00	9.47E-01	1.86E-02
4.00E+00	1.14E+00	1.99E-02
6.00E+00	1.32E+00	2.18E-02
8.00E+00	1.49E+00	2.49E-02

Table 1.05 Lift coefficient and Drag coefficient VS. angle of attack at ξ=60%

(Mach= 0.106, Rey= 625500)

a	C_l	C_d
-4.00E+00	2.47E-01	3.29E-02
-2.00E+00	5.00E-01	1.78E-02
0.00E+00	7.14E-01	1.65E-02
2.00E+00	9.17E-01	1.68E-02
4.00E+00	1.11E+00	1.83E-02
6.00E+00	1.27E+00	2.40E-02
8.00E+00	1.38E+00	3.35E-02

Table 1.06 Lift coefficient and Drag coefficient VS. angle of attack at ξ=70%

(Mach=0.121, Rey=794000)

a	C_l	C_d
-4.00E+00	1.77E-01	2.91E-02
-2.00E+00	4.12E-01	1.60E-02
0.00E+00	6.24E-01	1.53E-02
2.00E+00	8.23E-01	1.56E-02
4.00E+00	1.03E+00	1.68E-02
6.00E+00	1.21E+00	2.02E-02
8.00E+00	1.32E+00	3.00E-02

Table 1.07 Lift coefficient and Drag coefficient VS. angle of attack at ξ =80%

(Mach= 0.134, Rey= 868000)

a	C_l	C_d
-4.00E+00	1.25E-01	2.85E-02
-2.00E+00	3.65E-01	1.61E-02
0.00E+00	5.82E-01	1.47E-02
2.00E+00	7.93E-01	1.51E-02
4.00E+00	9.92E-01	1.64E-02
6.00E+00	1.16E+00	2.34E-02
8.00E+00	1.26E+00	3.83E-02

Table 1.08 Lift coefficient and Drag coefficient VS. angle of attack at ξ =90%

(Mach= 0.148, Rey= 938000)

a	C_l	C_d
-4.00E+00	1.25E-01	2.85E-02
-2.00E+00	3.65E-01	1.61E-02
0.00E+00	5.82E-01	1.47E-02
2.00E+00	7.93E-01	1.51E-02
4.00E+00	9.92E-01	1.64E-02
6.00E+00	1.16E+00	2.34E-02
8.00E+00	1.26E+00	3.83E-02

Table 1.09 Lift coefficient and Drag coefficient VS. angle of attack at ξ =96%

(C_l, and C_d are same to ξ =0.9)

a	C_l	C_d
-4.00E+00	1.25E-01	2.85E-02
-2.00E+00	3.65E-01	1.61E-02
0.00E+00	5.82E-01	1.47E-02
2.00E+00	7.93E-01	1.51E-02
4.00E+00	9.92E-01	1.64E-02
6.00E+00	1.16E+00	2.34E-02
8.00E+00	1.26E+00	3.83E-02

Table 1.10 Lift coefficient and Drag coefficient VS. angle of attack at ξ =100%

(C_l, and C_d are same to ξ =0.9)

V (knots)	Dynamic Pressure	J	?	C_T	C_P
8.689	0.255941	0.258753	0.382007	0.236711	0.160337
17.378	1.023763	0.517506	0.611981	0.206245	0.174406
21.7225	1.599629	0.646882	0.691934	0.188852	0.176556
26.067	2.303466	0.776259	0.758318	0.168139	0.172117
30.4115	3.135273	0.905635	0.813726	0.145245	0.16165
34.756	4.095051	1.035012	0.860441	0.120459	0.144898
36.92825	4.622928	1.0997	0.881003	0.107695	0.134429
39.1005	5.182798	1.164388	0.900194	0.094497	0.12223
41.27275	5.774661	1.229077	0.9182	0.080768	0.108114
43.445	6.398517	1.293765	0.935567	0.066127	0.091444

Table 2.01 CFD prediction of thrust coefficient, power coefficient and efficiency at fixed rotational speed (Specified RPM=400)

RPM	Dynamic Pressure	J	?	C_T	C_P
2000	4.095051	0.207106	0.3199	0.243558	0.157681
1500	4.095051	0.276141	0.400486	0.236301	0.162933
1000	4.095051	0.414212	0.53247	0.220589	0.171597
700	4.095051	0.591731	0.659026	0.197824	0.177624
600	4.095051	0.690353	0.71458	0.183564	0.17734
500	4.095051	0.828424	0.780643	0.160659	0.170492
400	4.095051	1.035529	0.859551	0.121735	0.146658
375	4.095051	1.104565	0.88147	0.108042	0.135387
350	4.095051	1.183462	0.904623	0.091789	0.120082
325	4.095051	1.274498	0.929373	0.071972	0.098699

Table 2.02 CFD prediction of thrust coefficient, power coefficient and efficiency at fixed flow speed (Specified Velocity=34.76 knots)

J	Experimental C_T	Computational C_T
0.2	0.22	0.244
0.4	0.198	0.221
0.6	0.185	0.192
0.8	0.158	0.162
1	0.122	0.126
1.1	0.102	0.109
1.15	0.092	0.095
1.2	0.08	0.085
1.3	0.05	0.064

Table 3.01 Comparison between numerical predictions and experimental measurements of thrust coefficient VS. advance ratio

J	Experimental C_P	Computational C_P
0.2	0.212	0.158
0.4	0.185	0.17
0.6	0.175	0.178
0.8	0.163	0.171
1	0.143	0.147
1.1	0.13	0.136
1.15	0.115	0.124
1.2	0.108	0.113
1.3	0.082	0.088

Table 3.02 Comparison between numerical predictions and experimental measurements of power coefficient VS. advance ratio

J	Experimental ?	Computational ?
0.2	0.2	0.3
0.4	0.412	0.515
0.6	0.63	0.661
0.8	0.752	0.76
1	0.836	0.851
1.1	0.858	0.881
1.15	0.87	0.894
1.2	0.854	0.908
1.3	0.76	0.936

Table 3.03 Comparison between numerical predictions and experimental measurements of efficiency VS. advance ratio